Available online at www.sciencedirect.com
SCIENCE DIRECT®
Journal of Nuclear Materials 350 (2006) 101–112
journal of nuclear materials
www.elsevier.com/locate/jnucmat

# Measurement of implanted helium particle transport by a flowing liquid lithium film

M. Nieto [a,1], D.N. Ruzic [a,*], W. Olczak [a], R. Stubbers [a,b]

[a] *Department of Nuclear, Plasma and Radiological Engineering, University of Illinois, 103 S. Goodwin Avenue, Urbana-Champaign, IL 61801, USA*
[b] *NPL Associates, Champaign, IL, USA*

Received 31 August 2004; accepted 26 September 2005

**Abstract**

Due to its low atomic number, low sputtering yield, high sputtered ion fraction and excellent thermal properties, liquid lithium has been proposed as a potential candidate for advanced plasma-facing components (PFC). Using a liquid material opens the possibility of a continuously flowing, self-regenerating plasma-facing surface with a small residence time. This would allow such component to handle very high heat loads that are expected. There are, however, multiple unanswered questions regarding how such a liquid PFC would interact with the plasma in the reactor. The issue of particle control is critical, and it can be a factor to determine the feasibility of these advanced concepts. Hydrogen and helium are important in this regard: hydrogen transport by a flowing PFC impacts the reactor fuel recycling regime and tritium inventory; helium transport can help quantify ash removal by the flowing PFC. The flowing liquid-metal retention experiment (FLIRE) was built at the University of Illinois to answer some of the questions regarding particle transport by flowing liquid films exposed to plasmas. Experimental results regarding helium transport by a flowing lithium film after irradiation with an energetic He ion beam are presented in this work. Retained fraction values up to 2% were measured for the experimental conditions, and the retention was found to increase linearly with implanted ion energy. A pure diffusion model was used to describe the helium transport by the Li film, and it was found that such model predicts a diffusion coefficient of $(2.8 \pm 0.6) \times 10^{-11}$ m$^2$/s, based on the experimental retention measurements. Preliminary evidence of long-term trapping of helium will also be presented.


*PACS:* 52.40.Hf; 66.10.Cb; 61.80.Jh; 41.75.Ak

## 1. Introduction

Plasma-facing components (PFCs) on tokamak fusion reactors are exposed to a considerable amount of energy flux. Typical reactor designs consider an average heat load to the wall close to 2 MW/m$^2$, but the ratio of peak to average thermal load is on the order of 50, and the peak occurs at the

* Corresponding author. Tel.: +1 217 333 0332; fax: +1 217 333 2906.
*E-mail address:* druzic@uiuc.edu (D.N. Ruzic).
[1] Present address: Argonne National Laboratory, Argonne, IL, USA.

0022-3115/$ - see front matter © 2005 Elsevier B.V. All rights reserved.
doi:10.1016/j.jnucmat.2005.09.028

divertor plate [1]. The heat load to internal components increases even more in the case of off-normal events, such as vertical displacements, edge-localized modes and disruptions [2–4]. Under these power fluxes, most materials would vaporize, and the particles coming from the divertor plate may find its way into the plasma core. This would cause radiative losses and fuel dilution, which both increase as $Z^2$, effectively reducing the reaction rate. Hence, low atomic number impurities are preferable.

Most tokamaks currently in operation use solid divertor plates, typically made out of graphite [5] or tungsten [6], which are materials that can withstand normal tokamak operating conditions. However, there are problems currently associated with the use of these solid materials:

(1) Solid divertors have very large exposure time to the plasma, they accumulate damage that may lead to ultimate failure after a certain period of time.
(2) Graphite divertors get eroded more rapidly than their metallic counterparts due to the chemical sputtering arising from the exposure to hydrogen plasmas [7].
(3) Tungsten, while having a very low sputtering yield for hydrogen, has a large atomic number that makes it an extremely undesirable impurity in the plasma since it can be sputtered by C or O readily and has a high self-sputtering coefficient. In addition it is hard to couple with other metals that serve as heat sinks such as copper [8].

In order to try to mitigate some of these problems, the use of materials that are already molten has been proposed. The use of liquids as divertor materials has some advantages over the use of solid components:

(1) The exposure time can be adjusted by the use of a flowing film or jet.
(2) Energy extraction can be done directly from the liquid outside the reactor.
(3) The component is not permanently damaged.
(4) Fuel trapped on the component can be extracted outside the reactor for reinjection.

There are, however, uncertainties in the use of liquid divertors. The effects of electric and magnetic field configurations on the flow of conducting liquids are not very well known. Fuel (hydrogen) and ash (helium) intake by the liquid may modify operation regimes of the reactor. Sputtering yield from the liquid may increase due to the increased temperature, enhancing impurity transport to the plasma [9].

Some of the liquids considered for divertor operation include molten metals and alloys such as lithium [10], tin and tin–lithium alloys [11,12], and gallium [13]; molten salts like FLiBE [14] have also been proposed as liquid divertor materials. Lithium is one of the leading candidates for liquid PFCs in tokamak reactors, due to its low atomic number, excellent thermal properties, its self-sputtering being less than 1, high sputtered ion fraction (2/3), and its ability to getter hydrogen to operate the reactor in a very low-recycling mode.

The Flowing Liquid-metal Retention Experiment (FLIRE) facility at the University of Illinois at Urbana-Champaign is aimed to help resolve one of the questions regarding liquid PFCs mentioned before; that is, the problem of quantifying hydrogen and helium transport when the liquid has been bombarded with energetic ions of such gases, as it would occur in the divertor of a real fusion reactor. Hydrogen transport is important in determining fuel recycling conditions, while helium transport is crucial for ash removal from the reactor volume. In the first step, which is reported here, an ion beam is used as plasma source in order to have a more controlled exposure of the fluid. FLIRE will be upgraded to study effects arising from the use of intense ion fluxes from a plasma impinging on the liquid metal.

## 2. Measurement of retention coefficient

The FLIRE facility was designed to allow the measurement of particles retained. A full description of the facility can be found elsewhere [15,16]. Two vacuum chambers, one on top of the other, are independently pumped and connected by a $3 \times 10$ mm rectangular slit, as shown in Fig. 1. The passage connecting the two chambers gets completely plugged when the liquid lithium flows between the two chambers. In the top chamber, the lithium stream can be exposed to a helium ion gun which usually requires backfilling with $10^{-2}$–$10^{-3}$ Pa of neutral gas to operate. The bottom chamber is furnished with a magnetic sector residual gas analyzer (RGA) capable of detecting partial pressures as low as $10^{-12}$ Pa.

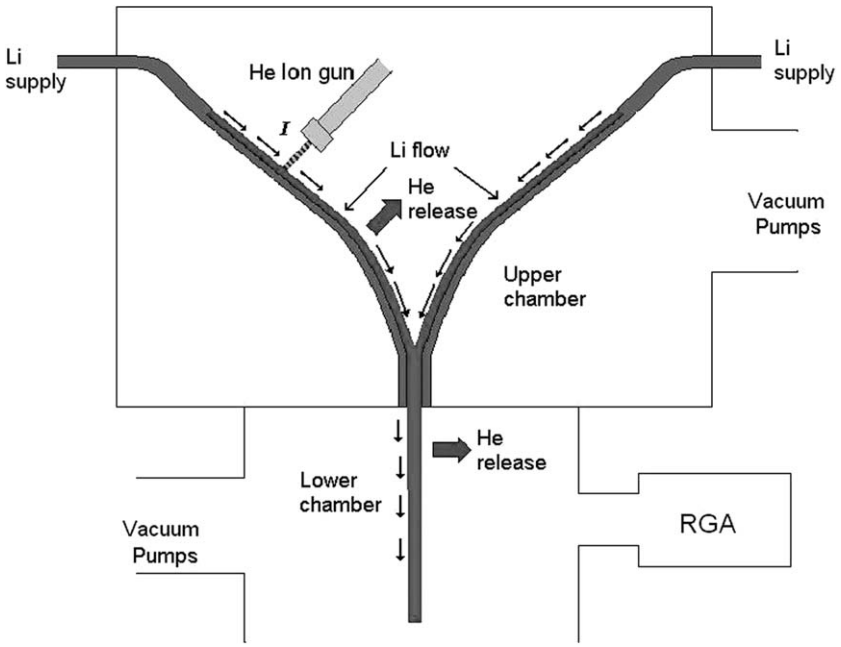


Fig. 1. The basic setup of FLIRE, showing the two chambers separated by a small passage. The passage gets plugged by the Li flow, allowing the RGA to measure only particles carried by the metal flow. Flow direction is indicated by the small arrows.

When a good coverage of the passage is achieved during the lithium flow, only the helium being desorbed from the metal can be detected in the lower chamber. To test if this condition can be achieved, experiments with the neutral pressure required for the ion gun in the upper chamber but the beam turned off were performed. The FLIRE upper chamber is filled with $10^{-2}$–$10^{-3}$ Pa of helium, and the lithium flows in the upper chamber for 40–50 s, but the ion source is not turned on, so that He particles are not implanted. The helium signal in the lower chamber for this experiment is shown in Fig. 2. It can be seen that the helium signal stays at background level while the lithium is flowing. This means that the chambers are adequately isolated from one another, since the neutral pressure in the upper chamber does not affect the signal in the lower chamber. The chambers remain isolated from each other even after the run is over, since the passage between the chambers is covered by lithium held there by surface tension. A pressure differential of 130 Pa or more is required to clear the connecting passage between the two chambers.

The next step is to measure the retained fraction when the gun is on. The retained fraction is dimensionless, and has to be related to the ratio of timescales. One time scale is the average diffusion time,

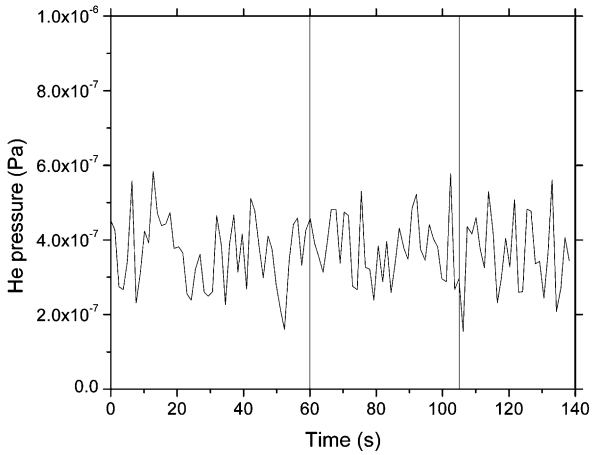


Fig. 2. Helium pressure trace in the lower chamber for an experiment where the ion gun was not turned on. Flow velocity is 0.7 m/s, and the flow lasts 45 s.

related to the implantation range and the diffusion coefficient. The other time scale is the transit time between the point of implantation and the exit from the upper chamber. This time scale is related to the flow velocity and the path length between the implantation point and the chamber exit. Hence, four parameters are key to determine the retained fraction:

(1) Flow velocity (faster flow means particles have less time to escape from the material, so the retained fraction increases with increased velocity).
(2) Path length in the upper chamber (shorter path length gives implanted particles less time to escape, so the retained fraction increases with decreased path length).
(3) Diffusion coefficient (fast diffusing particles escape the material easily, so retained fraction increases with decreased diffusion coefficient).
(4) Implantation range (deeper implantation means particles take longer to reach the surface, so retention fraction goes up with range).

The retention coefficient $R$ is defined as the ratio of total desorption rate in the lower chamber $q$ to implantation rate in the upper chamber $I$ (see Fig. 1):

$$R = \frac{q}{I}. \tag{1}$$

Eq. (1) is true only assuming that all the helium that remains inside the lithium escapes. If some is left behind, the value needs to be corrected. The issue of long-term retention will be discussed later in this work.

Fig. 3 shows the trace of helium in the lower chamber when a 1.5 keV, 1 μA ion beam is incident on lithium flowing at an average velocity of 0.7 m/s. Unlike Fig. 2, the helium signal in the lower chamber rises, but only when the ion gun is on, indicating that implantation is required in order to transport the helium and that the release in general is prompt. Vertical lines mark the start and the end of the flow, and the rise and fall of the helium signal is concurrent with the beginning and the end of the flow, respectively. The pressure values shown in the figures and those used in the calculation of the retention coefficient have been corrected for the difference in temperature at the ion gage and for the ionization efficiency of He vs. the $N_2$ calibration for the RGA.

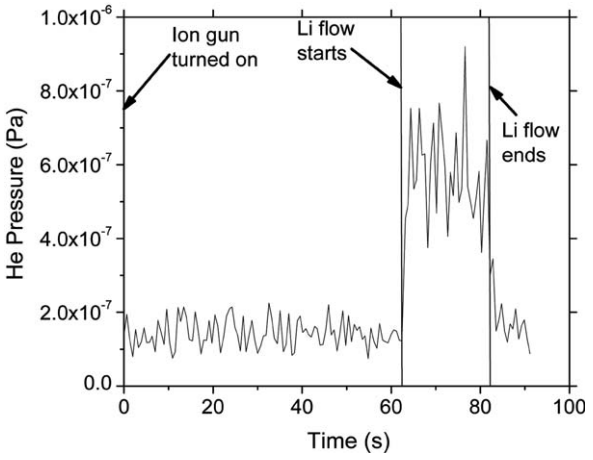


Fig. 3. Helium trace observed in the lower chamber when the lithium flow is bombarded by a He ion beam with an energy of 1.5 keV.

It can also be noted from Fig. 3 that a steady state pressure value (within some scatter) is achieved, so the release rate and the pumping rate of helium are equal. This equilibrium condition allows expressing the release rate in terms of the steady state helium partial pressure during the run, $P_{He}$, the pumping speed in the lower chamber, $S$, and the gas temperature $kT$ as

$$q = \frac{P_{He}S}{kT}. \tag{2}$$

The retention coefficient can then be obtained from measurable quantities:

$$R = \frac{P_{He}S}{IkT}. \tag{3}$$

The helium equilibrium pressure $P_{He}$ can be obtained from the RGA signal, the injection current $I$ is obtained from the calibration of the ion gun, the temperature of the measured gas $T$ is assumed to be room temperature, since the He atoms make many bounces from the chamber walls before getting detected, and the pumping speed $S$ can be measured by observing the exponential decay of the pressure after exposure to a small helium leak. In previous work, the uncertainty in these last parameters was very big, leading to unreliable retention values [17]. The system was modified to reduce the uncertainty in the pumping speed measurement drastically. Use of a turbomolecular pump instead of a cryogenic pump helped resolve the pumping speed measurement issues encountered in the past.

The helium ion current was determined during calibration of the ion source. The measured ion current is shown in Fig. 4 for an operating pressure of $1.3 \times 10^{-2}$ Pa and different values of the electron emission current on the source ionizer. The current was corrected for secondary ion emission using the following expression:

$$I_{ion} = \frac{I_{Tot}}{1+\gamma}. \tag{4}$$

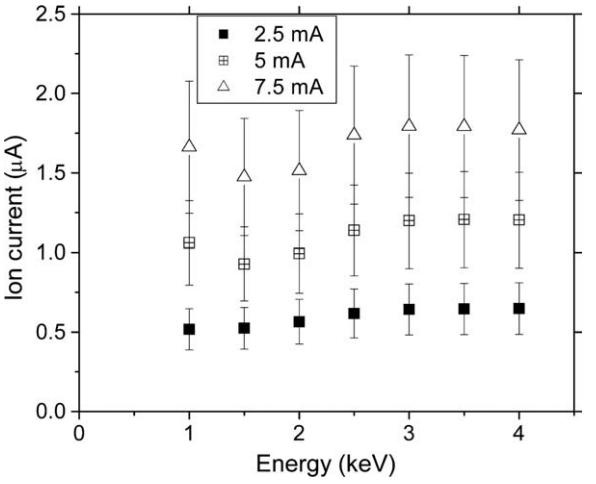


Fig. 4. The measured He ion current at $1.3 \times 10^{-2}$ Pa of helium for three different values of filament emission current and different beam energies.

Ion-impact secondary electron emission coefficient $\gamma$ data available in the literature [18] was used to correct the measured current. The current was found to be linear with both pressure and emission current, so values for other pressure and emission values can be found from Fig. 4. The error in the current arises from fluctuations in the emission current during ion gun operation. These fluctuations are 25% of the nominal emission value at a maximum, so an error of 25% is assigned to the current.

From Eq. (2), it is clear that the equilibrium pressure is inversely proportional to the pumping speed. For a given release rate, the equilibrium pressure increases with decreased pumping speed. For small release rates, such as the ones expected in this experiment, a small pumping speed is necessary to obtain a large signal-to-noise ratio on the pressure measurement. The reduction of the pumping speed is achieved by partial closure of the pump gate valve. Tests were made in order to determine the optimum pumping speed, and almost complete closing of the gate valve was necessary to achieve the right pumping speed. At such openings, small changes in the valve position may affect the pumping speed significantly. Hence, pumping speed measurements were performed after each set of experiments by injecting a small amount of helium into the lower chamber and observing the He signal decay. An exponential fit to this data gives the pumping speed $S$, since the signal decay has the following form:

$$P(t) = P_{\text{bckg}} + P_0 \cdot \mathrm{e}^{-\frac{S}{V}t}. \tag{5a}$$

Eq. (5a) can be rewritten as follows to facilitate the analysis of the data:

$$\ln(P(t) - P_{\text{bckg}}) = \ln P_0 - \frac{S}{V}t. \tag{5b}$$

Here, $P(t)$ is the measured He pressure at time $t$, $P_{\text{bckg}}$ is the background He pressure in the system, $P_0$ is the initial He pressure before the pumping starts, $V$ is the chamber volume and $S$ is the pumping speed. Since the volume of the chamber $V$ is known, the pumping speed can be obtained from the time constant of the decay, $S/V$. Upon fitting the model of Eq. (5b) to the data, a value of $(4.2 \pm 0.6) \times 10^{-4}$ m$^3$/s is obtained for the pumping speed. The pumping data, along with the fitted exponential decay, are shown in Fig. 5.

A set of experiments was performed to verify the expected trend of the retained helium fraction. They were performed at constant temperature (230 °C) and average flow velocity (0.7 m/s), and with the helium beam energy varied between 500 and 4000 eV in 500 eV intervals. At least two experimental measurements were taken for each value of the energy to improve the statistics. The helium pressure in the upper chamber was set to $1.3 \times 10^{-2}$ Pa and the filament emission of the ion source set to 5 mA, such that the ion current values for each energy are very similar to the ones in Fig. 4. The helium pressure evolution in the lower chamber during experiments with beam energies of 1, 2 and

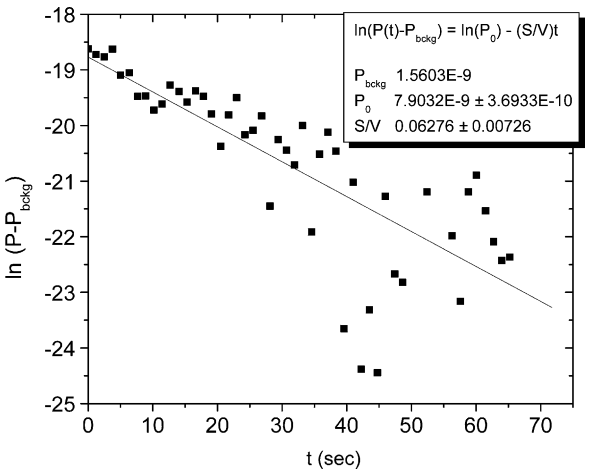


Fig. 5. Pumping curve for helium in the lower chamber, showing a fit of the form of Eq. (5b). The pressure drops exponentially, and the decay constant can be used to calculate the pumping speed. The parameters of the fit are the background pressure $P_{\text{bckg}}$, the initial pressure $P_0$ and the time constant for the decay $S/V$.

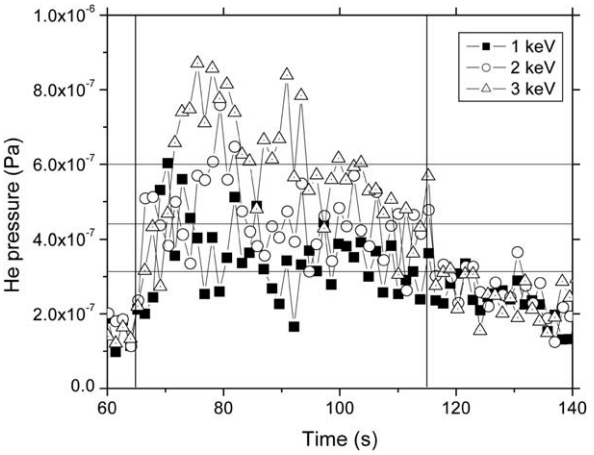


Fig. 6. Helium pressure traces in the lower chamber obtained when a lithium flow at 230 °C with velocity of 0.7 m/s is bombarded by a beam with different energy. Horizontal lines in the plot show the average value of the pressure during the time the liquid lithium is flowing, delimited by the vertical lines.

3 keV is shown in Fig. 6. As in the case of Fig. 3, the pressure reaches a plateau during the lithium flow. The pressure plateau level increases with energy, and the increase is not due to changes in the value of the current (see Fig. 4). The average value of the pressure during the length of the run is also shown in the figure. The error on the pressure plateau measurement is obtained from the standard deviation of the pressure data points within the flowing time; as the energy decreases, the signal-to-noise ratio gets smaller and hence the uncertainty of the measurement increases. The pressure plateau values for the whole set of experiments are presented in Fig. 7. It can be seen that the release rate (directly proportional to the pressure) increases with increasing energy, which is consistent with the expected behavior of the retention coefficient due to the higher implantation range. From Eq. (2), it is clear that values of the pumping speed are needed in order to convert from pressure to release rate. Multiplying the data from Fig. 7 by the corresponding value of pumping speed previously obtained, and dividing by $kT$ for $T$=25 ± 1 °C, the release rate is calculated. Dividing the release rate by the corresponding ion current, the retained fraction can be finally found, and a plot of $R$ vs. $E$, also shown in Fig. 7, is obtained. Since it was already shown that zero energy corresponds to zero retained fraction, a straight line fit with zero intercept is done to the retention data in Fig. 7, of the form $R = KE$. The parameter $K$ is found to be $(5.3 \pm 0.3) \times 10^{-3}$ keV$^{-1}$, particular for this set of experimental conditions, namely flow velocity, path length on the irradiation chamber and lithium temperature. This fact will be more evident once the model for implanted helium transport is discussed in the following section.

Another set of experiments was performed in order to determine if the ion current intensity had any effect on the retained fraction. For this second set, the experimental conditions were the same as those for the data presented so far, except the emission current for the source was increased from 5 to

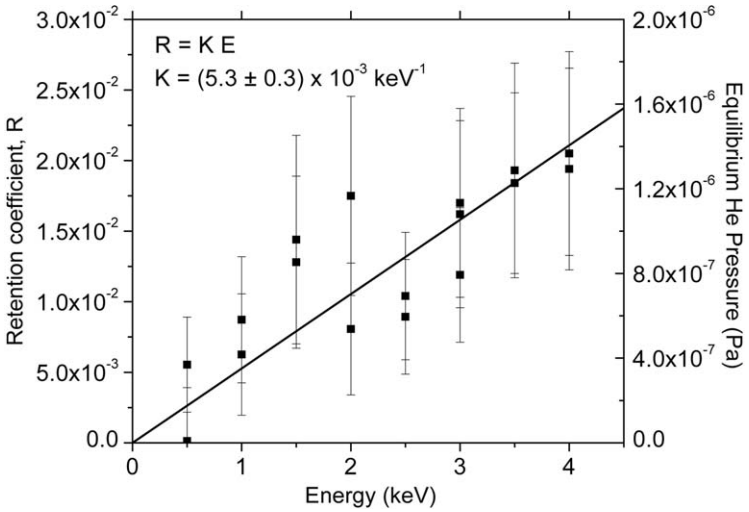


Fig. 7. Variation with energy of the steady state helium pressure in the lower chamber (right axis) and the retention coefficient calculated using Eq. (3) (right axis). Both quantities increase linearly with energy.

7.5 mA, increasing the ion current by the corresponding factor (50%) as shown in Fig. 4. The procedure used to calculate the retention coefficient was identical to the one discussed previously. Another measurement of the pumping speed using the technique described previously was done to account for a possible mismatch between the two sets of experiments after the second set was obtained. The pumping speed in this case was calculated to be $(3.3 \pm 0.2) \times 10^{-4}$ m$^3$/s. This value is slightly different from the one for the previous set, but the small difference indicates that the valve opening is very similar for both sets.

Fig. 8 presents the values of the release rate for the two sets of experiments, along with linear fits for both of them and their corresponding slopes values, $m_A$ for the lower ion current and $m_B$ for the higher ion current. Notice that the slope is higher for the high current set, indicating that higher desorption occurs in that case. From Eq. (3), dividing the release rate by the incident current gives the retention coefficient values, presented in Fig. 9 for this second set, along with the results from Fig. 7 for the previous set. Notice that the slope difference observed in Fig. 8 for the two sets of experiments has been greatly reduced; the slope obtained for the second set is $(6.0 \pm 0.3) \times 10^{-3}$ keV$^{-1}$, which is similar to the value obtained for the previous set. This fact seems to suggest that the retained fraction is not dependent on the current intensity, at least for the ion current levels used in this work. It can also be seen from Fig. 9 that the retained fraction

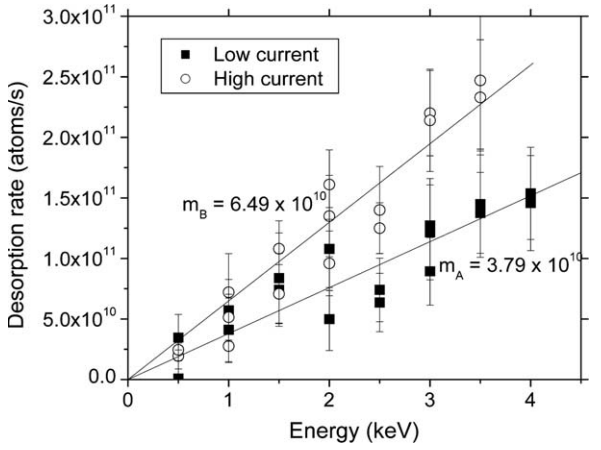


Fig. 8. Desorption rate calculated from Eq. (2) for two different sets of experiments, with all parameters the same except the ion current, which was 50% higher for one set. Slope values for the linear fits of the two sets are shown. Upon dividing this data by the ion current, retention values are obtained.

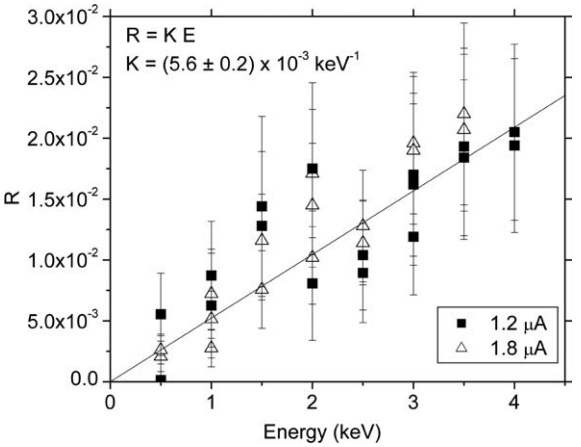


Fig. 9. Retention coefficient values as a function of energy for the two sets of data. The two sets have very similar slopes, indicating that the retention does not depend on the incident ion current.

increases linearly with the beam energy, indicating that it is proportional to the implanted particle range as expected. Combining the two results from the experiments gives an average value for $K$, $(5.6 \pm 0.2) \times 10^{-4}$ keV$^{-1}$.

## 3. Model to describe the helium transport

A model for the transport of implanted helium has been described in a previous work [17] and also by other authors [19,20]. It relies on finding the solution to the following partial differential equation:

$$\frac{\partial n}{\partial t} = D\frac{\partial^2 n}{\partial x^2} + G(x,t). \tag{6}$$

Here, $n$ is the concentration of helium atoms, $x$ is the distance normal to the flow measured from the surface into the flowing film, $G$ is the volumetric source of helium arising from the implantation and $t$ is the time elapsed for the observer. Eq. (6) neglects any diffusive transport parallel to the flow and also any turbulent flow effects, so the only mechanism for helium transport in the direction normal to the flow is diffusion. This partial differential equation is written for a Lagrangian frame of reference, where the observer moves along with the flow. Transformation to the Eulerian frame of reference is straightforward if constant flow velocity is assumed, since for that case the time elapsed for the Lagrangian observer $t$ is then equivalent to the distance traveled by the flow $y = vt$ for the Eulerian observer.

The boundary conditions for the differential Eq. (6) are

$$\begin{aligned} &n(0,t) = 0, \\ &\lim_{x\to\infty} n = 0, \\ &n(x,0) = 0. \end{aligned} \tag{7}$$

The first boundary condition states that helium is not soluble, so the concentration at the surface is always zero. The second assumes that the thickness of the film is much larger than the typical length scales for diffusion and implantation. The initial ($t = 0$) boundary condition states that there is no helium present prior to the implantation.

Regarding the source term $G$, the simplest form of it assumes that all the current is delivered instantaneously and that all particles are implanted at the mean range:

$$G(x,t) = \frac{I}{Wv}\delta(x-r)\delta(t). \tag{8}$$

Here, $I$ is the implantation current in atoms/s, $W$ is the width of the flow (a parameter which will be eliminated later), $v$ is the flow velocity and $r$ is the mean range of the implanted particles. The Dirac delta functions $\delta(t)$ and $\delta(x-r)$ represent the assumptions of instantaneous implantation and implantation at a unique depth, respectively. These two assumptions can be removed by replacing the two delta functions with a normalized implantation profile $f(x)$ and an implantation history $g(t)$ representing a spatial beam profile, also normalized:

$$G(x,t) = \frac{I}{Wv}f(x)g(t). \tag{9}$$

By using the method of Green's function [21] the general solution to Eq. (6) is given by

$$\begin{aligned} n(x,t) = \frac{I}{Wv}\int_0^\infty f(\xi)\Bigg[\int_0^t \frac{g(\tau)}{\sqrt{4\pi D(t-\tau)}} \\ \times\left[\exp\left(-\frac{(x-\xi)^2}{4D(t-\tau)}\right)\right. \\ \left.-\exp\left(-\frac{(x+\xi)^2}{4D(t-\tau)}\right)\right]\mathrm{d}\tau\Bigg]\mathrm{d}\xi. \end{aligned} \tag{10}$$

The amount carried into the lower chamber, which is assumed to be equal to the desorption rate, is calculated by integrating the concentration profile over the area normal to the direction of the flow $A_\perp$, given by $W\cdot x$. Since the width $W$ is constant, the integration to be performed is then:

$$q(t) = v\int_{A_\perp} n(x,t)\,\mathrm{d}A_\perp = vW\int_0^\infty n(x,t)\,\mathrm{d}x. \tag{11}$$

By using Eqs. (1), (10) and (11), the retained fraction can then be calculated from the following expression:

$$\begin{aligned} R(t)O = \int_0^\infty\Bigg\{\int_0^\infty f(\xi)\Bigg[\int_0^t \frac{g(\tau)}{\sqrt{4\pi D(t-\tau)}} \\ \times\left[\exp\left(-\frac{(x-\xi)^2}{4D(t-\tau)}\right)\right. \\ \left.-\exp\left(-\frac{(x+\xi)^2}{4D(t-\tau)}\right)\right]\mathrm{d}\tau\Bigg]\mathrm{d}\xi\Bigg\}\mathrm{d}x. \end{aligned} \tag{12}$$

The effects of the implantation profile and the beam spatial profile have been studied and found to be small corrections for the conditions in these particular experiments [16]. Hence, the assumptions that $g(t) = \delta(t)$ and $f(x) = \delta(x-r)$, where $r$ is the average range of the particle is valid. The integration of (12) is then straightforward and it yields:

$$R = \mathrm{erf}\left(\sqrt{\theta}\right). \tag{13}$$

The parameter $\theta$ is given by

$$\theta = \frac{r^2}{4Dt}. \tag{14}$$

The time $t$ is just equal to the distance traveled in the upper chamber $L$ divided by the flow velocity $v$. Then the resulting expression for the parameter $\theta$ is

$$\theta = \frac{vr^2}{4DL}. \tag{15}$$

Since the error function increases with $\theta$, it is clear that the retained fraction follows the expected trends if the parameters $v$, $r$, $D$ and $L$ are changed.

## 4. Estimations of the helium diffusion coefficient in liquid lithium

According to the model, the retained fraction is given by Eq. (13), which involves the error function. To avoid having to calculate the inverse error function, a linear approximation can be used, since the argument $\theta$ of the error function is very small, on the order of 0.01 or less for the experimental parameters used in this work. It can be approximated by the following straight line:

$$R = \mathrm{erf}\left(\sqrt{\theta}\right) \approx 1.13\cdot\sqrt{\theta} \quad \text{for } 0 < \theta < 0.01. \tag{16}$$

If the values of $R$ are available, the diffusion coefficient can be calculated as

$$D \approx \frac{1.28vr^2}{4LR^2}. \quad (17)$$

In the preceding section, the retained fraction $R$ was determined from the experimental measurements:

$$R = K \cdot E. \quad (18)$$

The mean range is linear with the energy, and for the case of helium particles incident in a lithium target it is given by

$$r = ((2.5 \pm 0.25) \times 10^{-8}\ \mathrm{m/keV})E. \quad (19)$$

Substituting Eqs. (18) and (19) into Eq. (17), the diffusion coefficient is then given by

$$D = (2.0 \pm 0.4) \times 10^{-16} \frac{v}{K^2 L}. \quad (20)$$

The diffusion coefficient $D$ from Eq. (20) is in units of $m^2/s$ if $v$ is given in m/s, $L$ is given in m and $K$ in $keV^{-1}$.The average flow velocity $v$ in the experiments was set to $0.7 \pm 0.06$ m/s, and the distance from the beam striking point to the exit of the upper chamber $L$ is fixed at $0.11 \pm 0.05$ m. The constant $K = (5.6 \pm 0.2) \times 10^{-3}\ keV^{-1}$ was determined in the previous section from the retention data. Use of these numbers yields a value for the diffusion coefficient of $(4.1 \pm 0.7) \times 10^{-11}\ m^2/s$. The individual values of the diffusion coefficient, $D$, along with the value derived by the method described here are shown in Fig. 10.

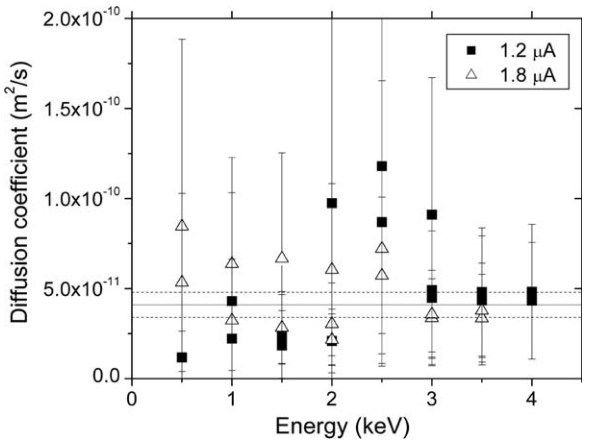


Fig. 10. Diffusion coefficient as a function of energy. The horizontal lines represent the average value for all the points, along with its error margin.

The value obtained for the diffusion coefficient seems small compared to values obtained for Nb and V at 500 K, on the order of $10^{-9}\ m^2/s$ [22]; however, diffusion of He in Mg, Al and steel is on the order of $10^{-14}$–$10^{-16}\ m^2/s$ [23–25], smaller than the value obtained in the present work. Unfortunately, diffusion data for He in liquid metals is not very abundant, so a direct comparison cannot be made. Nonetheless, the experiment described here simulates the appropriate system. What is needed to determine the effectiveness of He pumping by a flowing liquid lithium film is direct measurement of diffusion from a flowing liquid lithium film. The fact that the effective diffusion coefficient for such a system is small brings benefits from the point of view of the helium pumping efficiency, since the retention increases by a factor of 10 compared to previous estimates using diffusion coefficients that are 100 times higher [19]. It should also be noticed that the qualitative behavior of the retention seems to agree with the simple diffusion model. More advanced models that include other effects such as flow turbulence, surface impurities or bubble nucleation need to be developed in order to identify the mechanism responsible for the enhanced retention.

## 5. Long-term release of helium

In order to verify if indeed all the helium comes out of the lithium, some annealing experiments were performed, in order to accelerate the release if some helium is still inside the metal. The experiments involved the heating of the lithium charge, first without exposing it to the beam to verify if any helium was trapped, and then after exposing it to the beam to determine how important this fraction is. Note that if a significant amount of He was trapped in a long-term manner, the diffusion coefficient calculated in the previous section would be even *smaller* and the opportunity to pump He using flowing Li in a fusion device would be even greater.

Fig. 11 shows the He pressure signal in the lower chamber for the annealing experiments of the lithium charge flowing through the upper chamber without being exposed to the beam, only to the typical operating He pressure. Once the whole charge was in the lower chamber, it was heated to 360 °C, soaked at that temperature for 10 min and then cooled back down to 230 °C. The black solid line in the Figure shows the temperature evolution during heating and cooling. When the temperature reaches 320 °C, a series of small spikes in the He

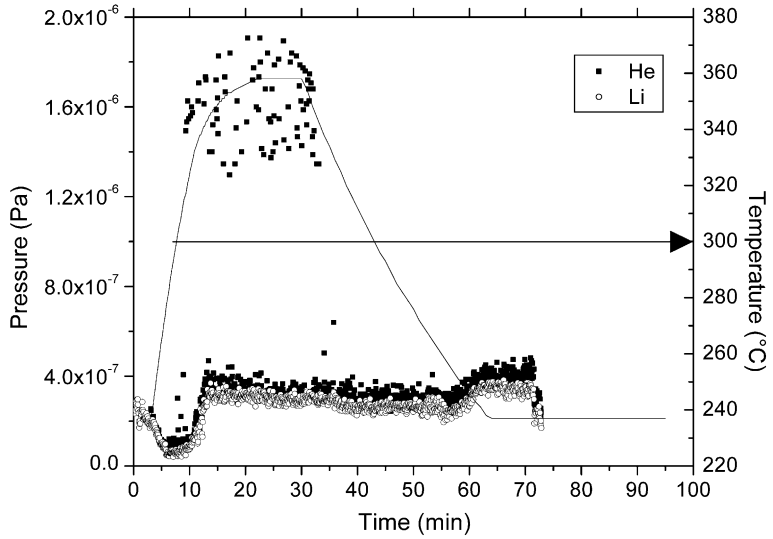


Fig. 11. Helium trace in the lower chamber during thermal annealing of the lithium charge. The solid line shows the temperature history. No implantation was done on this charge, and helium is released as a series of pressure bursts that occur once a critical temperature is reached, indicated by the arrow.

pressure start to appear, and they continue to be present until the temperature drops below 320 °C during the cool-down phase. The frequency distribution of pressure spike intensity is presented in Fig. 12, and it can be seen that the distribution of spikes can be fitted with a normal distribution centered around $8 \times 10^{-6}$ Pa and a standard deviation of $9 \times 10^{-7}$ Pa.

Since the bubbles disappeared upon cooling, the same experiment was repeated with this lithium charge after flowing it through the system once more, again with no implantation. The temperature treatment was repeated, and bubble release was observed again (Fig. 13). However, this time the bubbles drop in number drastically during the soaking phase, and they eventually die away. This may indicate the total removal of residual helium from the charge.

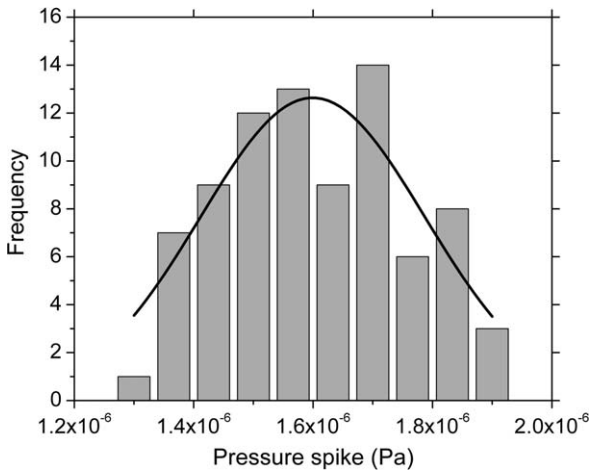


Fig. 12. Distribution of the pressure spikes in Fig. 12. Solid line shows a normal distribution fit.

Once the charge went through the two annealing cycles, and indication that the residual helium was removed, the charge was now exposed to a 1.2 μA 3 keV He ion beam. The same heating treatment was done to the charge, and bubbles were present again, but not with the same intensity as in the two previous treatments, as can be seen from Fig. 14. Both prompt and delayed release can be observed, and in order to compare their relative magnitudes, integration over the time was done. The prompt release rate $q_P$, is calculated as before:

$$q_P \propto P_{avg} t_{run}. \tag{21}$$

$P_{avg}$ is the average pressure reached during the prompt release phase ($1.2 \times 10^{-7}$ Pa in this case), and $t_{run}$ is the running time of the flow, which was 45 s. For the delayed release, the release rate was calculated as

$$q_D \propto \delta t \sum_{i=1}^{N_B} P_{spike,i}. \tag{22}$$

The sum of all the pressure spikes $P_{spike}$ is multiplied by the time resolution of the measurement

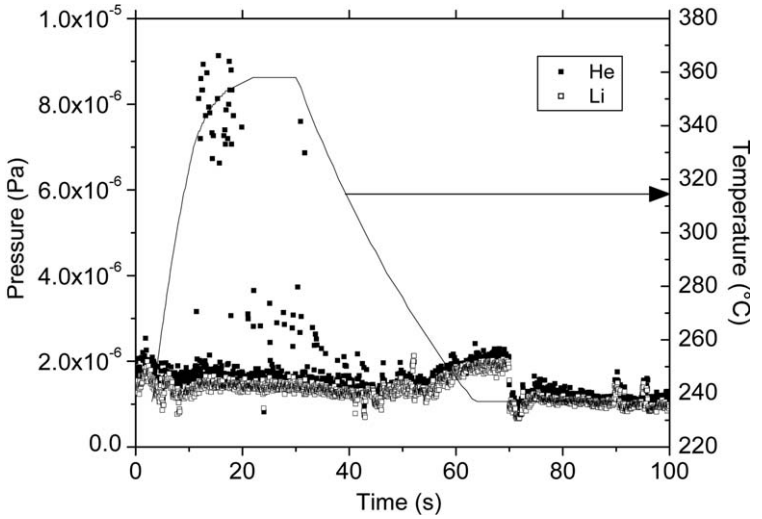


Fig. 13. Helium release during the second annealing of the Li charge. Pressure spikes are observed again, but their intensity starts to decay halfway into the treatment.

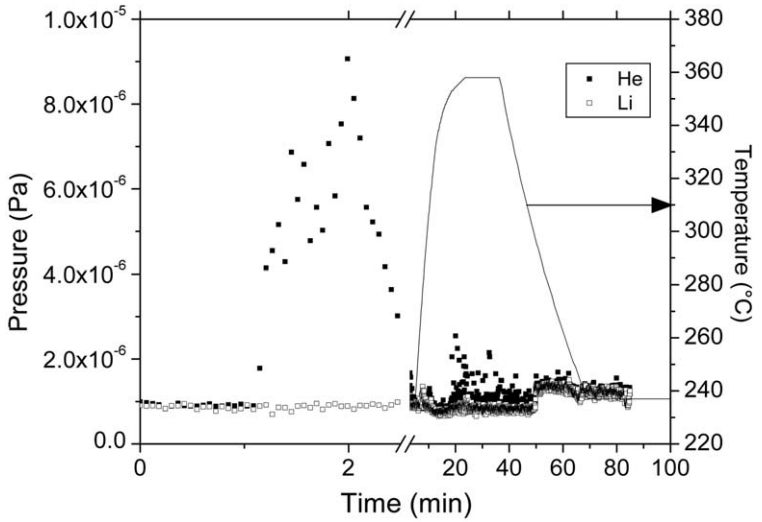


Fig. 14. Helium release from a lithium charge exposed to a helium ion beam. The continuous prompt release is observed between 1 and 2 min, while the discrete long-term release is observed after 10 min and only when the lithium charge has been heated past 300 °C.

$\delta t$, which is 3.5 s. If the proportional constants are assumed to be equal for both cases, then the amount of helium that was trapped in the metal can then be calculated as

$$\frac{\left(\frac{\delta t}{t_{\text{run}}}\right)\sum P_{\text{spike}}}{P_{\text{avg}}+\left(\frac{\delta t}{t_{\text{run}}}\right)\sum P_{\text{spike}}}. \tag{23}$$

In this case, the fraction of the delayed release turns out to be 20%, assuming that all the residual helium from previous exposure of the charge was removed during the two thermal treatments previous to this last experiment.

## 6. Conclusions

The transport of implanted helium by a flowing film of lithium was measured in the FLIRE facility. It was found that the retained fraction increases linearly with energy, as it was predicted by the model. The retained fraction as a function of energy was

given by $R = E\cdot(5.6 \pm 0.2) \times 10^{-3}\ \mathrm{keV}^{-1}$. Measurements of the retained fraction allowed the calculation of the diffusion coefficient based on the model described in this work. The diffusion coefficient for He in Li at 230 °C was found to be $(2.8 \pm 0.6) \times 10^{-11}\ \mathrm{m}^2/\mathrm{s}$. Such a small diffusion coefficient for a liquid metal indicates that this value is not likely a true diffusion coefficient, but an effective one that includes some mechanism that enhances the helium retention. Such mechanism still needs to be identified, but possibilities include turbulent transport, helium nucleation or surface layers that may act as diffusion barriers. However, it is this effective diffusion coefficient that is relevant for a fusion-energy-related system.

Preliminary work regarding the quantification of long-term He trapping in the metal was performed. It was observed that the release of trapped He is in the form of bubbles, which have a normal distribution of sizes, and such release is only observed upon heating the sample. There is a release threshold in temperature of 320 °C, which either corresponds to the value of the diffusion coefficient necessary to increase mobility and allow nucleation or represents an activation energy to release He from lithium oxide or lithium nitride 'scale' along the sides of the chamber. This issue of long-term retention, once quantified systematically, will further increase the overall retention of helium, but further studies are necessary in order to make a better quantification.

## Acknowledgments

This work was supported by the US Department of Energy grant # DE-FG02-99ER54515, as well as NPL subcontract DOEANL02-160. Special thanks to Keith Thompson, Ian Treviranus, Jason Tillery, Gabriel Burt, Daniel Rokusek, Sarfraz Taj, Frank Wonda, Helger Meier, Daniel Schultz, Alvin Thalappillil and Jason Draper for helping in the completion of this work.

## References

[1] M.A. AbdouAPEX Team, Fus. Eng. Des. 45 (1999) 145.
[2] A. Hassanein, I. Konkashbaev, J. Nucl. Mater. 290–293 (2001) 1074.
[3] A. Hassanein, Fus. Eng. Des. 60 (2002) 527.
[4] H. Würz, B. Bazylev, I. Landman, S. Pestchanyi, Nucl. Instrum. and Meth. A 415 (1998) 543.
[5] J.P. Coad, B. Farmery, Vacuum 45 (1994) 435.
[6] A. Cambe, E. Gauthier, J.M. Layet, S. Bentivegna, Fus. Eng. Des. 56&57 (2001) 331.
[7] D. Alman, D.N. Ruzic, J. Nucl. Mater. 313–316 (2003) 182.
[8] I. Smid, M. Akiba, G. Vieider, L. Plochl, J. Nucl. Mater. 258–263 (1998) 160.
[9] J.P. Allain, M.D. Coventry, D.N. Ruzic, J. Nucl. Mater. 313–316 (2003) 641.
[10] J.N. Brooks, T.D. Rognlien, D.N. Ruzic, J.P. Allain, J. Nucl. Mater. 290–293 (2001) 185.
[11] K. Natesan, W.E. Ruther, J. Nucl. Mater. 307–311 (2002) 743.
[12] M.A. Fütterer, G. Aielloa, F. Barbierb, L. Giancarlia, Y. Poitevina, P. Sardainc, J. Szczepanskia, A. Li Pumaa, G. Ruvutusod, G. Vellad, J. Nucl. Mater. 283–287 (2000) 1375.
[13] N.B. Morley, M.A. Abdou, Fus. Eng. Des. 30 (1995) 339.
[14] T.D. Rognlien, M.E. Resnick, J. Nucl. Mater. 290–293 (2001) 312.
[15] J.P. Allain, M. Nieto, M.D. Coventry, M.J. Neumann, E. Vargas-Lopez, D.N. Ruzic, Fus. Eng. Des. 61&62 (2002) 245.
[16] M. Nieto, PhD thesis, University of Illinois at Urbana-Champaign, 2004.
[17] M. Nieto, J.P. Allain, M.D. Coventry, E. Vargas-Lopez, D.N. Ruzic, J. Nucl. Mater. 313–316 (2003) 646.
[18] B. Szapiro, J.J. Rocca, T. Prabhuram, App. Phys. Lett. 53 (1988) 358.
[19] A. Hassanein, J. Nucl. Mater. 302 (2002) 41.
[20] C. Liao, M.S. Kazimi, J.E. Meyer, Fus. Technol. 23 (1993) 208.
[21] J. Kevorkian, Partial Differential Equations: Analytical Solution Techniques, Chapman & Hall, New York, NY, 1990.
[22] M.B. Lewis, J. Nucl. Mater. 152 (1988) 114.
[23] R. Vassen, H. Trinkaus, P. Jung, J. Nucl. Mater. 183 (1991) 1.
[24] A.J.E. Foreman, B.N. Singh, J. Nucl. Mater. 141–143 (1986) 672.
[25] H. Trinkaus, J. Nucl. Mater. 118 (1983) 39.